ACS NANO

www.acsnano.org

ARTICLE

Localized Excitons in $NbSe_2$-$MoSe_2$ Heterostructures

Jaydeep Joshi, Tong Zhou, Sergiy Krylyuk, Albert V. Davydov, Igor Žutić, and Patrick M. Vora*

Cite This: *ACS Nano* 2020, 14, 8528−8538

Read Online

ACCESS | Metrics & More | Article Recommendations | Supporting Information

ABSTRACT: **Neutral and charged excitons (trions) in atomically thin materials offer important capabilities for photonics, from ultrafast photodetectors to highly efficient light-emitting diodes and lasers. Recent studies of van der Waals (vdW) heterostructures comprised of dissimilar monolayer materials have uncovered a wealth of optical phenomena that are predominantly governed by interlayer interactions. Here, we examine the optical properties in $NbSe_2$-$MoSe_2$ vdW heterostructures, which provide an important model system to study metal−semiconductor interfaces, a common element in optoelectronics. Through low-temperature photoluminescence (PL) microscopy, we discover a sharp emission feature, L1, that is localized at the $NbSe_2$-capped regions of $MoSe_2$. L1 is observed at energies below the commonly studied $MoSe_2$ excitons and trions and exhibits temperature- and power-dependent PL consistent with exciton localization in a confining potential. This PL feature is robust, observed in a variety of samples fabricated with different stacking geometries and cleaning procedures. Using first-principles calculations, we reveal that the confinement potential required for exciton localization naturally arises from the in-plane band bending due to the changes in the electron affinity between pristine $MoSe_2$ and $NbSe_2$-$MoSe_2$ heterostructure. We discuss the implications of our studies for atomically thin optoelectronics devices with atomically sharp interfaces and tunable electronic structures.**

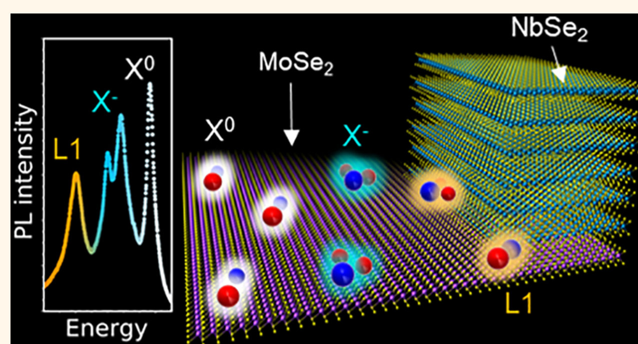

KEYWORDS: *excitons, van der Waals heterostructures, transition metal dichalcogenides, photoluminescence, density functional theory*

Semiconductor heterostructures are key to modern technology and devices such as transistors, lasers, solar cells, and light-emitting diodes.[1] However, the growth constraints of lattice matching between different semiconductors significantly limit not only the number of semiconductor heterostructures but also their ultimate performance and functionality. These constraints can be overcome with the growing number of two-dimensional (2D) crystals in which different atomic monolayers (MLs) are coupled by weak van der Waals (vdW) forces. Stacking 2D crystals leads to vdW heterostructures which are immune from growth rules, capable of forming atomically sharp interfaces, and also transform materials physics through proximity effects.[2] In fact, even transition metal dichalcogenides (TMDs), a small subset of these 2D crystals, embody a wide range of materials properties, including being semiconducting, metallic, magnetic, superconducting, or topologically nontrivial.[3−6] The electronic structure in TMDs combines time-reversal symmetry and broken inversion symmetry, which has important implications for optical and transport properties. Semiconducting ML TMDs have direct band gaps,[7] very large excitonic binding energies (up to 0.5 eV),[8] efficient light emission,[9,10] and a characteristic coupling between the K and K′ valleys and the carrier spin.[11]

An important opportunity for vdW heterostructures lies in the potential to interface layered materials with dissimilar properties, dimensionality, and lattices, a capability that could enable complex device functionalities impossible with conventional materials.[12,13] Unfortunately, TMD-based devices with common metals often lead to highly resistive contacts[14−17] and limit the possibility to effectively combine different materials including the opportunity to employ desirable proximity effects.[2] Furthermore, such metals are typically also responsible for a rapid decay of charge carriers from the semiconductor, resulting in significant quenching of photoluminescence (PL) emission,[18−20] constraining their use in TMD-based optoelectronic devices.

Received: April 2, 2020
Accepted: July 8, 2020
Published: July 8, 2020

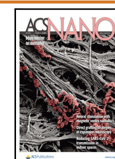

Downloaded via GEORGE MASON UNIV on January 29, 2021 at 01:01:04 (UTC).
See https://pubs.acs.org/sharingguidelines for options on how to legitimately share published articles.

© 2020 American Chemical Society

https://dx.doi.org/10.1021/acsnano.0c02803
ACS Nano 2020, 14, 8528−8538

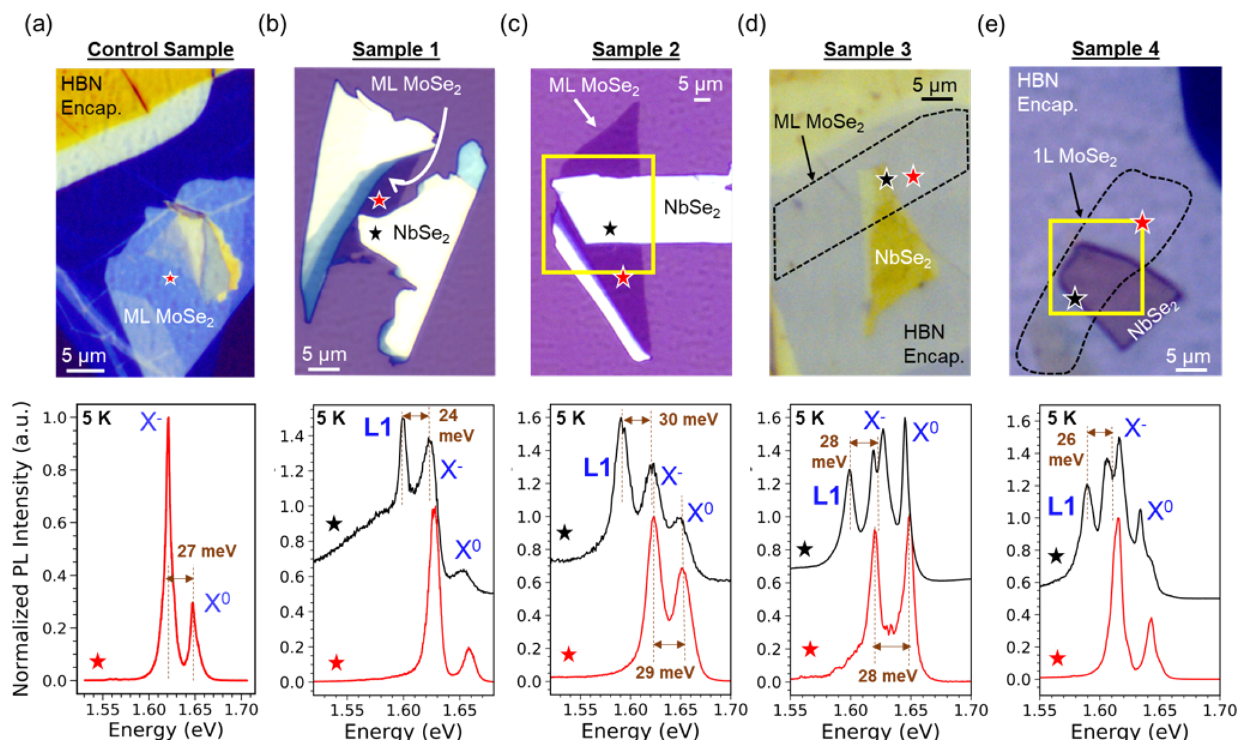

Figure 1. White light images of (a) ML-$MoSe_2$ control sample and (b−e) samples 1, 2, 3, and 4 comprising of $NbSe_2$-$MoSe_2$ vdW heterostructures. Samples 1 and 2 are fabricated on Si/SiO_2 substrate, whereas samples 3 and 4 as well as the control sample are fully encapsulated with few-layer hexagonal boron nitride (hBN). The black dotted line in (d) and (e) outlines the ML-$MoSe_2$ region. Beneath each image are low-temperature PL spectra taken on (black) and off (red) the $NbSe_2$-$MoSe_2$ interface. These locations are denoted by red and black stars in the white light image. The yellow boxes mark the regions scanned in hyperspectral PL maps. In addition to the X^0 and X^- emission observed in samples 1−4, a PL feature referred to as L1 appears at ≈1.6 eV in all heterostructures.

A promising direction to solve these obstacles relies on using atomically thin metals to create low-resistance and highly transparent vdW contacts. Particularly interesting are Nb-based metallic TMDs which offer low, p-type Schottky barriers with many 2D semiconductors in addition to exhibiting superconductivity.[21−25] This has enabled further developments in fabricating ultrathin devices, where drastic changes in the electronic landscape of the $NbSe_2$ contact can modulate the channel carrier properties of the transistor.[24,26−28] On the other hand, extensive investigations to understand interfacial contact properties and nearby dielectrics in $MoSe_2$-based metal−semiconductor heterostructures has helped engineer efficient optoelectronic devices.[29−32] However, despite this progress in the studies of 2D metal−semiconductor heterostructures, important uncertainties in their optical properties and the role of excitons remain. Fermi level pinning at metal−semiconductor interfaces can induce midgap states in the semiconductor, thereby enabling additional radiative channels for exciton recombination.[33−37] Semiconducting ML TMDs pose additional challenges with the influence of surrounding dielectric media, where 2D metals can drastically change the exciton dynamics as well as the ability to effectively screen electrons in the semiconductor.[38]

Motivated by the promising properties of $NbSe_2$-based contacts with semiconducting TMDs as well as their largely unexplored optical response, we perform hyperspectral and temperature- and power-dependent PL spectroscopy of heterostructures composed of bulk-$NbSe_2$ and ML-$MoSe_2$. A PL feature (labeled L1) consistently appears between 1.59 eV and 1.6 eV, approximately 25−30 meV below the $MoSe_2$ trion and is far more sensitive to temperature changes than other excitonic emissions, while it exhibits a sublinear excitation-power dependence. This feature is robust even under very different assembly conditions (observed across 10 samples) and present only at the metal−semiconductor interface. We explain L1 as a localized exciton state in deep potential well traps provided by an in-plane band-offset between the pristine $MoSe_2$ and its region capped by $NbSe_2$. We find that a particular fabrication procedure of $NbSe_2$-$MoSe_2$ heterostructures results in high-quality interfaces that facilitate the observation of moiré intralayer excitons and trions created by the bulk $NbSe_2$ moiré potential. The implications of L1 for emerging vdW-based optoelectronic devices are discussed.

RESULTS AND DISCUSSION

Optical Characterization of vdW Heterostructures. White light images of a subset of $NbSe_2$-$MoSe_2$ vdW heterostructures and a control sample are presented in Figure 1. The control sample (Figure 1a) consists of ML-$MoSe_2$ fully encapsulated with few-layer hexagonal boron nitride (hBN). Samples 1 and 2 are assembled directly on a Si/SiO_2 substrate without encapsulation, as shown in Figure 1b,c. Samples 3 and 4 (Figure 1d,e) are both fully encapsulated with few-layer hBN, with ML-$MoSe_2$ regions outlined by dashed black lines. Below each image are low-temperature (5 K) PL spectra showing emissions on (black star) and off (red star) the $NbSe_2$-$MoSe_2$ interface shown in the corresponding image. All samples exhibit PL features close to 1.65 and 1.62 eV attributed to neutral exciton (X^0) and negatively charged trion (X^-) emissions in ML-$MoSe_2$, respectively.[39] We expect the trion to be X^- and not X^+ owing to the formation of Se vacancies

https://dx.doi.org/10.1021/acsnano.0c02803
ACS Nano 2020, 14, 8528−8538

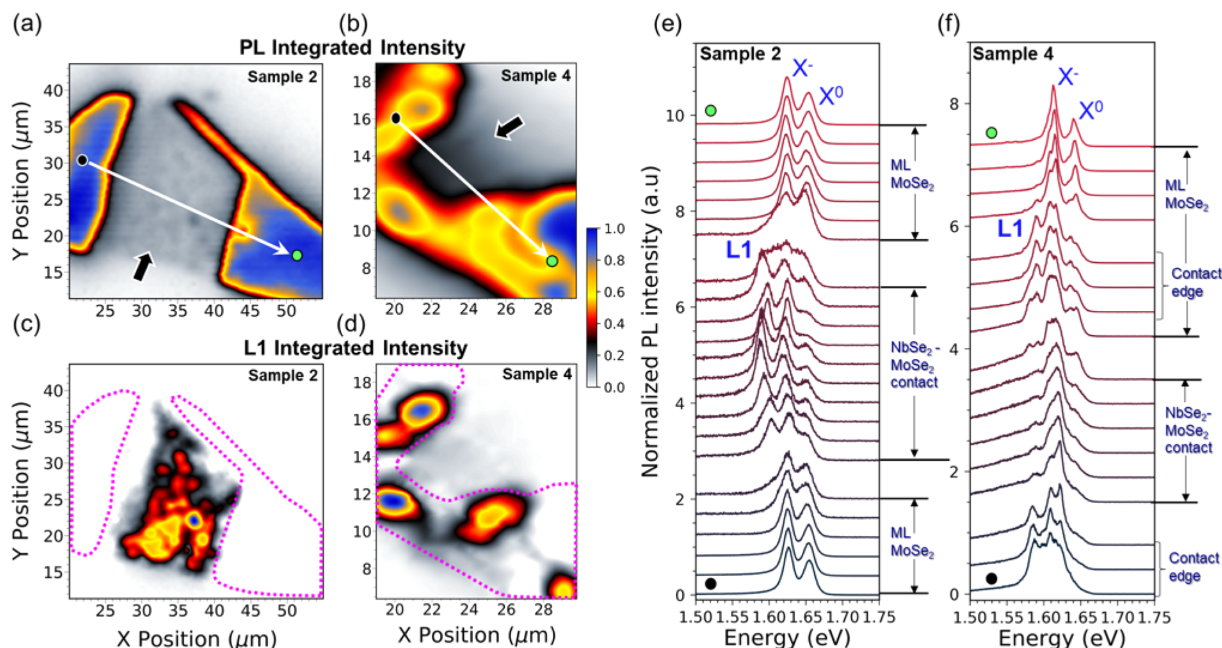

Figure 2. Low-temperature hyperspectral maps of the integrated PL intensity from 1.5 eV to 1.7 eV for (a) sample 2 and (b) sample 4 and integrated PL intensity of L1 peak for (c) sample 2 and (d) sample 4. The regions scanned correspond to the yellow boxes in Figure 1. White arrow in panels (a) and (b) corresponds the path of the linecuts examined in (e) and (f). The magenta dashed outlines in panels (c) and (d) mark pristine ML-MoSe$_2$. PL spectra extracted along the linecuts in (a) and (b) plotted for (e) sample 2 and (f) sample 4. L1 is localized along the NbSe$_2$-MoSe$_2$ perimeter in sample 4, while it appears across the NbSe$_2$-MoSe$_2$ interface in sample 2. The black and green dots refer to the start and end positions of the linecuts, respectively.

and anti-sites during synthesis as well as the tendency of chemical vapor transport (CVT) grown MoSe$_2$ to be inherently n-type.[40] Extrinsic doping effects from polymer residue and the plasma-cleaned Si/SiO$_2$ substrate likely also contribute to the presence of X$^-$. The observed X$^-$ binding energy (≈ 27−30 meV) and PL line widths (≈4−6 meV for samples 3 and 4, ≈6−9 meV for samples 1 and 2) are consistent with prior measurements,[39,41−44] and their variation is likely due to dielectric tuning of the Coulomb interaction after hBN encapsulation.[38,45,46]

The most obvious difference between on (black) and off (red) spectra is the appearance of an additional PL peak close to ≈1.6 eV, about 25−30 meV lower than the X$^-$ peak. The intensity and line width of this peak, hereafter referred to as L1, varies between samples, however, its energy with respect to the X$^-$ peak remains unchanged and its emission localized to the NbSe$_2$-MoSe$_2$ interface. L1 is also surprisingly robust to the quality of the interfacial contact between the two TMDs, as demonstrated by its presence in 10 of the 14 heterostructures created in this study (see Supporting Information (Figure S1)) with a variety of stacking configurations and post-assembly cleaning procedures (see Methods section). The four samples where we do not observe L1 have suffered from excessive polymer residue and/or oxidation of NbSe$_2$. Furthermore, X^0 and X$^-$ PL peaks split in hBN-encapsulated samples 3 and 4 (Figure 1d,e), which results in a five peak structure at the NbSe$_2$-MoSe$_2$ interface. We believe this to be a consequence of intralayer moiré exciton at the interface formed between NbSe$_2$ and MoSe$_2$, similar to the observations in MoSe$_2$-MoS$_2$ heterostructure (discussed in Supporting Information (Figure S2)).[47]

Hyperspectral PL measurements allow us to understand the spatial origin of L1 and determine whether vdW coupling between NbSe$_2$ and MoSe$_2$ has any contribution. Figure 2a,b here shows the spatially mapped integrated PL intensity acquired at 5 K for samples 2 and 4 (hBN-encapsulated), respectively, across the area marked by yellow boxes in Figure 1c,e. The black arrows indicate regions of NbSe$_2$-MoSe$_2$ overlap. We first examine the variation in integrated PL intensity (total sum of X^0, X$^-$, and defect emission), where, compared to the bright emission observed from the uncapped region, a reduction by a factor of 5 is seen at the overlap between NbSe$_2$ and MoSe$_2$ flakes. However, the fact that any PL signals are recorded from the NbSe$_2$-capped regions suggests that nonradiative relaxation into NbSe$_2$ is a weaker process than might be expected. The reduction in the total PL intensity at the interface is likely due to the combined reflection of the incoming laser and MoSe$_2$ PL by the capping NbSe$_2$ layer, although substrate interference effects may also play a role.[48] Figure 2c,d shows variation in the integrated intensity of L1 (method outlined in Supporting Information (Figure S3)) measured across the same area. These maps highlight an important difference between the behavior of L1 in encapsulated and unencapsulated samples. As seen in Figure 2c, for sample 2 fabricated without hBN-encapsulation, L1 is present over the majority of the NbSe$_2$-MoSe$_2$ interface. This is in contrast to the hBN-encapsulated sample 4, where L1 is more prominent over the perimeter of the NbSe$_2$-MoSe$_2$ region (Figure 2d). The impact of interface quality can be made more apparent by examining PL plots of spectra extracted along a linecut, depicted by the white arrow that extends over the interface from the pristine MoSe$_2$ regions in Figure 2a,b. The black and green dots represent the starting and ending points of the linecut, respectively. It is clear from Figure 2e (sample 2) that as we move from ML-MoSe$_2$ to the region in contact with NbSe$_2$, L1 appears at about 30 meV below the X$^-$ peak. In contrast to sample 2, Figure 2f shows that L1 is more pronounced along the edges surrounding the

https://dx.doi.org/10.1021/acsnano.0c02803
ACS Nano 2020, 14, 8528−8538

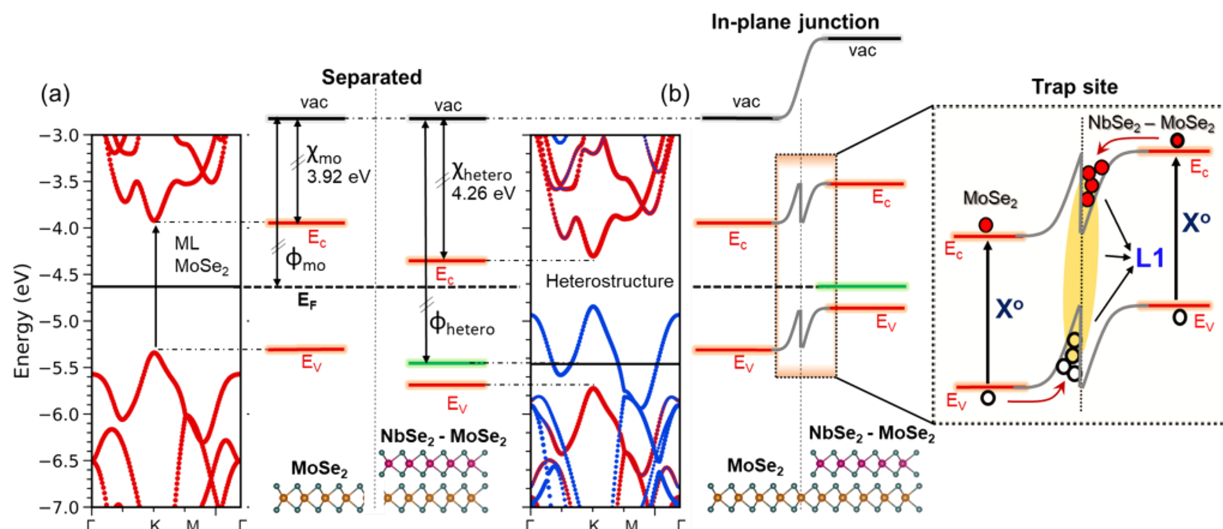

Figure 3. (a) A schematic of changes in the work function (Φ) and electron affinity (χ) between $NbSe_2$-$MoSe_2$ contact and pristine $MoSe_2$ traced from their respective DFT calculated band structures. Red bands derive from $MoSe_2$, while blue bands derive from $NbSe_2$. The *Y*-axis for both band structures is scaled such that the zero energy refers to the vacuum energy. (b) Discontinuous band bending allows for the formation of potential traps at the in-plane junction as the Fermi level (E_F) matches between the two region. A zoom in at the junction shows confinement of electrons and holes in the valence band (VB) and conduction band (CB) of capped and uncapped $MoSe_2$. L1 PL emission then occurs due to the recombination of trapped electrons and holes (yellow).

$NbSe_2$-$MoSe_2$ overlap in sample 4 than at the interface. Additionally, for both samples, we see a clear broadening of the X^0 and X^- PL peaks near the interface compared to the pristine $MoSe_2$ region. This is typical for metal−semiconductor junctions where rapid decay of charge carriers can result in reduced exciton lifetimes and inhomogeneously broadened PL line widths. The difference in the spatial distribution of L1 in sample 2 *versus* sample 4 over the $NbSe_2$-$MoSe_2$ interface is likely due to variable coupling between the flakes. Sample 4 was processed with a "nano-squeegee" technique[49] (see Methods) and then annealed in vacuum which produces a clean, uniform interface. Sample 2 was only vacuum annealed which redistributes polymer residue to form larger bubbles and some well-coupled regions.[50−53] The different spatial distribution of L1 in these samples requires a deeper understanding regarding vdW coupling between $NbSe_2$ and $MoSe_2$.

$NbSe_2$-$MoSe_2$ Contact: First-Principles Calculations. In this section, we focus on understanding and distinguishing the origin of the L1 peak from previously studied low-energy optical pathways in ML-$MoSe_2$. We begin by presenting a brief survey of explorations to engineer $MoSe_2$ exciton states, multiexciton $MoSe_2$ states, and excitons in $MoSe_2$-based vdW heterostructures and discuss how L1 defies explanation by these prior works. The controlled application of strain to ML-$MoSe_2$ was found to induce localized quantum emitters with ultrasharp PL line widths over a wide range of energies below X^0 and X^-.[54] While an attractive explanation, L1 exhibits a PL line width that is much broader than a strain-induced quantum emitter and a consistent emission energy of ≈1.6 eV, disagreeing with discrete quantum dot picture. On the other hand, a broad low-energy feature (between 1.5 and 1.6 eV) appears in the gate-dependent PL measurement of pristine ML-$MoSe_2$, but is associated with impurity trapped excitons with line widths an order of magnitude larger than X^0, X^-, and L1.[39] We may also exclude the possibility of $NbSe_2$-induced activation of dark exciton states based on the recent observation of the $MoSe_2$ dark neutral exciton, which lies 1 meV above X^0 and is therefore spectrally well-separated from L1.[41] Strain-dependent measurements on ML-$MoSe_2$ have revealed a uniform red shift in the X^0 and X^- peak energies, without the appearance of low-energy emission features.[55] Measurements to probe higher-order exciton complexes such as neutral or charged biexcitons have revealed features at energies lower than the X^0, however their binding energies do not match the spectral position of L1.[56] Finally, the emergence of interlayer valley excitons in $MoSe_2$-based vdW heterostructures occurs at about 1.3−1.4 eV much lower than our observation of L1.[57] Therefore, we can conclude that L1 originates from an interaction between $NbSe_2$ and $MoSe_2$.

In order to quantify the interaction between $NbSe_2$ and $MoSe_2$, we perform first-principles calculations of the $NbSe_2$-$MoSe_2$ heterostructure. Density functional theory (DFT) calculations are presented in Figure 3 for the pristine and heterostructure system. Here, Figure 3a illustrates the ML-$MoSe_2$ band structure (left plot, red bands) which hosts a direct band gap at the *K* point in agreement with previous calculations.[58,59] The calculated electron affinity of ML-$MoSe_2$ is χ_{Mo} = 3.92 eV, and the Fermi level (E_F) and work function (Φ_{Mo}) are set midgap based on the assumption of an undoped ML in agreement with recent work.[60] Bandstructure calculations for a ML-$NbSe_2$-ML-$MoSe_2$ heterostructure are also presented in Figure 3a (right plot) where the blue (red) bands derive from $NbSe_2$ ($MoSe_2$) orbitals, respectively, and qualitatively match prior modeling efforts of this system.[25] We note that although the top $NbSe_2$ flake is bulk (60−100 nm) in our case (Supporting Information Figure S9), our use of ML-$NbSe_2$ in these calculations is sufficient to capture the essential physics of the system as vdW interactions weaken for additional layers. Also included in the Supporting Information (Figure S4) is the electronic band structure for ML-$NbSe_2$ which is metallic with a calculated workfunction value of Φ_{Nb} = 5.56 eV, in agreement with previous work.[61] Upon first examination, the $MoSe_2$ band structure is qualitatively unchanged by the presence of $NbSe_2$. The $MoSe_2$ bandgap (E_g) remains the same, and there is no band hybridization between the $MoSe_2$ and $NbSe_2$ orbitals except at the Γ point

https://dx.doi.org/10.1021/acsnano.0c02803
ACS Nano 2020, 14, 8528−8538

where there is a weak mixing. This mixing originates from the fact that Nb and Mo d-bands at the Γ point have an out of-plane (d_{z^2}) orbital character resulting in a weak hybridization, while the high-symmetry K point orbitals are largely in-plane (d_{xy}, $d_{x^2-y^2}$) and therefore less sensitive to the addition of $NbSe_2$. The lack of Mo−Nb band hybridization at K implies excitonic behaviors in $MoSe_2$ will remain in the heterostructure. Interestingly, the main impact of introducing $NbSe_2$ to $MoSe_2$ is a downward shift in the conduction and valence band energies by 0.34 eV, implying that the electron affinity for $MoSe_2$ in the heterostructure is χ_{hetero} = 4.26 eV. This band offset between pristine $MoSe_2$ and $NbSe_2$-capped region is a direct consequence of the vdW interaction, where an attractive potential offered by $NbSe_2$ relaxes the energy landscape of the semiconductor (details in Supporting Information (Figure S6)). These results are consistent with prior examinations of heterostructure where $NbSe_2$ is stacked upon a semiconductor.[21,25] Though seemingly minor, the observed change in electronic affinity χ between the two systems will be critical in explaining the origin of L1 peak.

It is important to note here that while Fermi levels can be tuned arbitrarily within the band gap of the semiconductor and are pinned by the metal in a metal−semiconductor junction, electron affinities associated with these regions are fixed and determine band alignment. In a scenario shown in Figure 3a, the values Φ and χ obtained from our first-principles calculations are used to illustrate an in-plane band schematic as one moves from the pristine $MoSe_2$ region to the $NbSe_2$-$MoSe_2$ overlap. As a consequence of charge rearrangement to electronically equilibriate ML-$MoSe_2$ and to match E_F across the two regions, the $MoSe_2$ bands in the two regions must bend at the interface. Since E_g does not change, band bending is determined by the differences between Φ and χ at the interface. Our DFT calculations indicate that the respective changes in these parameters are dissimilar which leads to a band alignment that hosts potential well traps for both electrons and holes as illustrated in Figure 3b. This in-plane confinement potential acts as a trap for excitons and trions where they then recombine and result in the L1 peak. This mechanism of interface trapping and recombination is known to produce an additional PL feature in AlGaAs/GaAs heterostructures referred to as an "H-band".[62] The trapping potential created by band bending provides a natural explanation for the hyperspectral PL maps presented in Figures 2c and 2d which correspond to samples 2 and 4 (hBN-encapsulated), respectively. Sample 2 was subjected to a vacuum annealing procedure post-assembly that consolidates residual polymer in a vdW heterostructure to form larger bubbles while providing some regions with pristine contact.[50−53] This results in a "patchy" vertical interface where the interlayer separation varies across the $NbSe_2$-$MoSe_2$ heterostructure. Traps will appear at any boundary between well-coupled and poorly coupled regions that in turn lead to L1 PL emission that varies over the $NbSe_2$-$MoSe_2$ contact (Figure 2c). In contrast, sample 4 is fully encapsulated in hBN and was subjected to the "nano-squeegee" cleaning technique where an AFM tip is used to physically remove polymer residue from the heterostructure.[49] This results in a more uniform spacing, and therefore coupling, between $NbSe_2$ and $MoSe_2$. Thus, the only regions that contribute to the band bending required to create a trapping potential are along the edge of the $NbSe_2$-$MoSe_2$ overlap. The resulting map of the L1 feature therefore should only show PL from the edge of $NbSe_2$ which is exactly the case

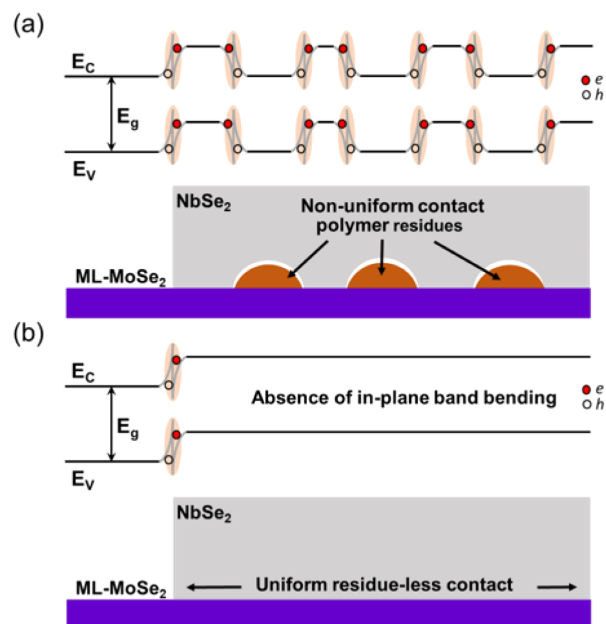

Figure 4. Spatially resolved band bending schematics. (a) Samples 1 and 2 have large polymer bubbles between $NbSe_2$ and $MoSe_2$ that create numerous in-plane boundaries between well-coupled and poorly coupled regions. PL from L1 is therefore expected from traps randomly distributed across the $NbSe_2$-$MoSe_2$ overlap. (b) Samples 3 and 4 were subjected to an additional cleaning step, "nano-squeegee", that provides a relatively polymer-free interface. L1 therefore only appears at the edge of $NbSe_2$-$MoSe_2$ overlap.

shown in Figure 2d. These two situations are schematically illustrated in Figure 4. We observe behavior consistent with this model in 10 of the 14 samples created in this study. In the remaining four samples, we do not observe L1 which we believe is due to a combination of excessive polymer residue or oxidation of $NbSe_2$.

We note that wrinkles, folds, and more general strain can lower the bandgap in ML-$MoSe_2$, leading to quantum-dot-like emission features.[54] While these prior observations do not resemble L1, we evaluate the impact of wrinkling in the Supporting Information (Figure S9). We observe that some wrinkles can indeed produce a peak similar to L1, however this is rare with other strained or structurally modified regions elsewhere on the same flake not producing L1-like PL spectra. Changes in the electronic band structure locally at wrinkled sites can introduce a funnel effect where excitons can drift to from the pristine sections of the ML flake. These funnels are similar to in-plane traps discussed in this manuscript and have been observed in mechanically wrinkled ML-MoS_2.[63,64] Additionally, a before/after experiment illustrates the importance of the vdW coupling in sample 5 (Supporting Information (Figure S10)). Hyperspectral PL maps of the pristine, undamaged ML-$MoSe_2$ flake before the stamping of $NbSe_2$ show no signs of L1, even on torn regions of the flake. Upon the stamping of $NbSe_2$, we find that L1 appears at the $NbSe_2$-$MoSe_2$ boundary. This proves that L1 is not a direct product of any surface abnormality in the plane of ML-$MoSe_2$ and rather originates strictly from manipulations of the electronic landscape by a well-coupled bulk-$NbSe_2$ flake.

Localized Nature of L1. The present physical model implies that L1 originates from the recombination of excitons, and possibly trions, trapped in a confinement potential created by band bending between $MoSe_2$ and $NbSe_2$-$MoSe_2$ regions.

https://dx.doi.org/10.1021/acsnano.0c02803
ACS Nano 2020, 14, 8528−8538

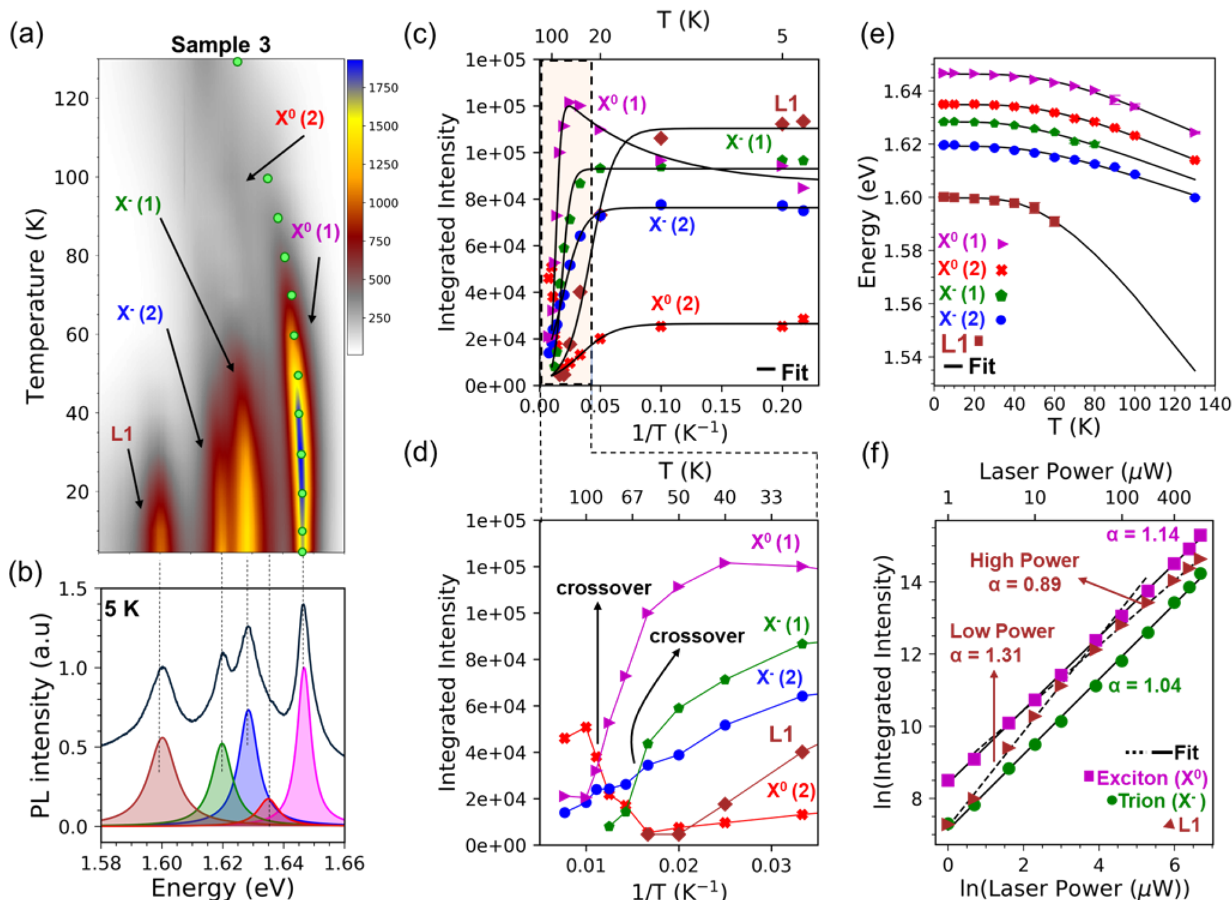

Figure 5. (a) Temperature-dependent PL intensity map for sample 3 on the $NbSe_2$-$MoSe_2$ interface. We identify five distinct transitions: L1, $X^0(1)$, $X^0(2)$, $X^-(1)$, and $X^-(2)$. Green dots denote the temperatures where spectra were taken. (b) PL scan at 5 K with an example fit to five Lorentzians. (c) Temperature-dependent integrated PL intensity of the peaks in (b). The black line is a fit to eq 1. (d) A zoom-in of the temperature-dependent integrated PL intensity from 30 to 130 K. A crossover between high- and low-energy moiré excitons and trions is observed. (e) PL peak energies extracted from the fits in (b) *versus* temperature. Marker colors match the fill colors for specific Lorentzians in (b), and the black line is a fit to eq 2. One σ error bars are included. (f) Natural logarithm of the integrated intensity of L1, X^0 and X^- features *versus* the natural logarithm of the laser power at the $NbSe_2$-$MoSe_2$ interface in sample 3. The black solid and dotted lines are power-law fits to the data with the power α indicated for the high-power and low-power regions. $\alpha < 1$ for L1 at high powers.

L1 should therefore exhibit the characteristics of a localized exciton in temperature- and power-dependent PL measurements. Prior observations of localized excitons in 2D materials show they disappear quickly with increasing temperature and exhibit a sublinear power dependence due to the saturation of all available trap sites.[65,66] We find that L1 exhibits both of these characteristics, as shown in Figure 5. Temperature-dependent PL measurements on the $NbSe_2$-$MoSe_2$ interface in sample 3 are presented in Figure 5a. Similar data for sample 1 is included in Supporting Information Figure S5. We observe that L1 is thermally quenched above 60 K in contrast to X^0 and X^-. This is in agreement with the localized exciton picture, where a thermal energy greater than the trapping potential can eject confined charge carriers through nonradiative mechanisms. Sample 3 has been subjected to an extensive cleaning procedure and is encapsulated in hBN, which results in the observation of five peaks in total compared to samples fabricated on Si/SiO_2 substrates. These features are suspected to originate from intralayer moiré potentials[47,67,68] and are elaborated upon in Supporting Information (Figure S2). We fit each spectrum to a combination of Lorentzian functions with a constant background from 1.55−1.7 eV to extract the emission energy and the integrated intensity of the observed PL features. These are plotted in Figure 5c−e as a function of temperature for peaks assigned as L1, $X^0(1)$, $X^0(2)$, $X^-(1)$, and $X^-(2)$ in keeping with the intralayer moiré exciton.[47] A representative Lorentzian fit is shown for the 5 K spectrum in Figure 5b, where the fill color of each peak corresponds to the marker colors in Figure 5c−e.

Temperature dependence of the integrated PL intensity provides key insight into the localized nature of L1. In TMDs with inherent defects and vacancies, thermal disassociation of trapped exciton can sometimes elevate the number of charge carriers available for radiative recombination, giving a rise in the exciton PL intensity up to a certain thermal threshold. We find that $X^0(1)$ exhibits such a nonmonotonic temperature-dependent intensity at the interface, as shown in Figure 5c. For all other peaks, we observe a monotonic behavior that follows the expectation for localized excitons. Temperature dependence of the integrated PL intensity can be fit with a modified Arrhenius formula:[69−71]

$$I(T) = I(0)\frac{1 + Ae^{-E_{a1}/k_B T}}{1 + Be^{-E_{a2}/k_B T}} \quad (1)$$

where $I(0)$ is the integrated PL intensity at T = 0 K, k_B is the Boltzmann constant, and A and B are fitting parameters used to

determine the ratio of radiative to nonradiative recombination rates of charge carriers. E_{a1} is the activation energy that increases the number of carriers available for recombination, and E_{a2} is the activation energy for the normal thermal quenching process at higher temperatures through nonradiative channels. $X^0(1)$ is fit extremely well by this model as shown in Figure 5c. For the remaining peaks in Figure 5c, all of which lie at a lower emission energy, we obtain good fits to eq 1 when $A = 0$, implying the remaining peaks are not enhanced by the thermal activation of additional carriers. This suggests that it is likely the thermal quenching of L1 that provides the carriers responsible for the rise in the temperature dependent intensity of $X^0(1)$. The fitting parameters for the temperature-dependent integrated PL intensity data are summarized in Table 1. The values of E_{a1} = 0.12 meV and E_{a2} = 37 meV for $X^0(1)$ and E_{a2} = 23 meV for $X^-(1)$ obtained from our fits agree with other studies of similar TMDs,[70,72,73] whereas for L1, a value of E_{a2} = 8.58 meV is extracted. We note that E_{a2} may be interpreted as the binding energy for $X^-(1)$, $X^-(2)$, $X^0(2)$, and L1. For $X^0(1)$, the model in eq 1 is not well constrained over the measured temperature range, as the neutral exciton is present well above 300 K. Therefore, E_{a2} is only a lower bound of the expected $X^0(1)$ binding energy. Furthermore, the value B, which relates to the ratio of nonradiative decay rate in the high-temperature limit to the radiative decay rate is also higher for L1 compared to $X^0(2)$ and $X^-(2)$ peaks, indicating a more favorable, nonradiative recombination process for confined states than the intralayer moiré states ($X^0(2)$ and $X^-(2)$) which are strongly protected by the interfacial geometry at the contact region. For $X^0(1)$ and $X^-(1)$, the higher values of B are a natural consequence of the abundance of free exciton and trion states that undergo nonradiative recombination due to scattering and exciton−exciton annihilation processes. We have included a similar analysis for a ML-$MoSe_2$ sample in the Supporting Information (Figure S7), where we cover a wider temperature range (5−300 K) and observe no anomalous increase in the intensity of X^0 with increasing temperature.

Table 1. Best-Fit Parameters of eq 1 to the Temperature-Dependent Integrated PL Intensity of Sample 3 (Figure 5c)

peak ID	E_{a1} (meV)	E_{a2} (meV)	A	B	$I(0)$
$X^0(1)$	0.12	37.14	0.56	342.47	86,209
$X^0(2)$	–	6.14	–	11.11	26,461
$X^-(1)$	–	23.75	–	171.37	92,999
$X^-(2)$	–	9.98	–	9.10	76,293
L1	–	8.58	–	64.80	110,334

Finally, we point out an interesting crossover in the intensities of the moiré intralayer excitons. In Figure 5d, we present the high-temperature region (30 K < T ≤ 130 K) of the temperature-dependent integrated intensity data. At low temperatures, we find that $X^0(1)$ and $X^-(1)$ dominate the spectrum. However, as temperature is increased, $X^0(2)$ and $X^-(2)$ gradually gain spectral weight and replace their higher energy partners. This behavior is consistent with the prior study of moiré intralayer excitons in MoS_2-$MoSe_2$ heterobilayers,[47] where a similar intensity crossover was observed and attributed to the thermally assisted relaxation of $X^0(1)$ and $X^-(1)$ into lower energy regions of the moiré potential. Our measurements are consistent with this mechanism and generally support our assignment of these features as moiré intralayer excitons. It is notable that prior studies have only explored moiré excitons in carefully assembled bilayer vdW heterostructures. The observations presented here indicate that moiré excitons should generally be expected between well-coupled layered materials, even when one is a bulk vdW metal.

In Figure 5e, the extracted peak energies are fit to a standard model that describes temperature-dependence of the semiconductor band gap,[39,74]

$$E_g(T) = E_g(0) - S\langle\hbar\omega\rangle\left[\coth\left(\frac{\langle\hbar\omega\rangle}{2k_BT}\right) - 1\right] \quad (2)$$

where $E_g(0)$ is the transition energy at T = 0 K, S is a dimensionless constant describing the strength of the electron−phonon coupling, and $\langle\hbar\omega\rangle$ represents the average acoustic phonon energy involved in electron−phonon interactions. We are able to fit all five observed peaks to this functional form and summarize the fitting parameters in Table 2. The obtained values for the dominant X^0-like and X^--like peaks agree reasonably well with previous study of pristine ML-$MoSe_2$.[39] L1 exhibits the highest value of S, which suggests substantial electron−phonon coupling and is consistent with its rapid thermal quenching.

Table 2. Best-Fit Parameters of eq 2 to the Temperature-Dependent Emission Energies of Sample 3 (Figure 5e)

peak ID	E_g (eV)	S	$\langle\hbar\omega\rangle$ (eV)
$X^0(1)$	1.646	2.41	0.018
$X^0(2)$	1.634	2.17	0.017
$X^-(1)$	1.628	1.76	0.012
$X^-(2)$	1.62	1.66	0.014
L1	1.60	6.97	0.017

Power-dependent measurements are presented for sample 3 in Figure 5f and for sample 1 in Supporting Information (Figure S5). We expect for the excitonic species a scaling of $I \propto P^\alpha$, where I is the integrated PL intensity and P is the excitation power and $\alpha \approx 1$ for single exciton complexes and <1 for localized trap-states.[65,66] For ease of analysis, we plot natural logarithms of the integrated PL intensity and excitation laser power and extract the coefficient (or slope) α for L1, X^0, and X^- peaks. In both cases (samples 1 and 3), we observe that X^0 and X^- peaks scale linearly with increasing power and the obtained values of α closely approximate to unity. In order to illustrate the sublinear behavior of the L1 peak, we have divided the power axes in two different regimes, and we fit its behavior in each range by a standard linear fit. In case of Figure 5f, the low-power regime (0 < P < 50 μW) shows an α value that closely matches that of the X^0, followed by the high-power regime (50 μW ≤ P ≤ 800 μW) where α is < 1. Similar trends are observed for sample 1 across the low- and high-temperature ranges. This is typical of a trapped state, where photoexcited carriers saturate trap sites and manifest as a change in the behavior of PL intensities at higher laser power, depicting an overall sublinear trend.

CONCLUSION

In this study we have identified a spectral feature, L1, in $NbSe_2$-$MoSe_2$ vdW heterostructures. We attribute this feature to a recombination of localized excitons trapped by in-plane confinement potentials formed between $NbSe_2$-$MoSe_2$ and $MoSe_2$. Both our first-principles calculations as well as the

https://dx.doi.org/10.1021/acsnano.0c02803
ACS Nano 2020, 14, 8528−8538

temperature- and power-dependent PL measurements support this interpretation. Surprisingly, even under widely different fabrication procedures of our heterostructures, L1 remains robust and appears consistently at ≈1.6 eV. We compare our findings to other low-energy emissions observed in $MoSe_2$-based vdW heterostructures and show that L1 originates from the geometry discussed in this manuscript, but may occur in a variety of metal−semiconductor heterostructures depending on the band offset between the pristine and capped semiconducting TMD regions. Moiré intralayer excitons are observed for hBN-encapsulated nano-squeegeed samples and suggest that moiré excitons should be generally expected in vdW heterostructures, even when one of the constituents is a bulk metal. The consistent PL energy of L1 may solve an outstanding problem of spectral inhomogeneity in 2D single-photon sources, where photon energies vary due to the different strain and defect-induced confinement potentials. Since metal−semiconductors interfaces are common building blocks for many optoelectronic devices,[75,76] we also envision extending our findings to systems which would explicitly take into account spin and valley degrees of freedom. For example, preserving similar robust optical properties in ferromagnetic metal−semiconductor heterostructures could be an important step in realizing 2D spin lasers that in common III−V semiconductors can exceed the performance of the best conventional lasers.[77] Furthermore, with high-quality and tunable interfacial properties, similar heterostructures would be an important platform in designing proximitized materials.[2]

METHODS

Growth of TMD Materials. $NbSe_2$ and $MoSe_2$ single crystals were grown by the CVT method. Polycrystalline $NbSe_2$ and $MoSe_2$ precursors were synthesized by reacting stoichiometric amounts of Nb (Mo) and Se powders in vacuum-sealed quartz ampule at 850 °C for 72 h. For $NbSe_2$, a quartz ampule containing about 1 g of $NbSe_2$ charge and ≈80 mg (3.7 mg/cm^3) of I_2 transport agent was sealed under vacuum and placed in a single-zone furnace. Temperatures at the charge and growth zones were T_{hot} = 825 °C and T_{cold} = 700 °C, respectively, and the growth duration was 140 h. 2H-$MoSe_2$ single crystals were grown using $SeBr_4$ transport agent (5 mg/cm^3) at T_{hot} = 980 °C and T_{cold} = 850 °C.

Sample Preparation, Assembly and AFM "Nano-Squeegee". MLs of 2H-$MoSe_2$ were obtained through mechanical exfoliation of as-grown crystals and subsequently transferred on O_2 plasma cleaned Si/SiO_2 substrates (samples 1 and 2) or encapsulated with few-layer hBN (samples 3 and 4) using the PDMS-based dry viscoelastic stamping method.[78] This method has been known to leave a polymer residue, but enables the straightforward and rapid fabrication of vdW heterostructures.[51] A similar procedure was employed to exfoliate and transfer bulk $NbSe_2$ flakes to assemble a heterostructure with bulk-$NbSe_2$-ML-$MoSe_2$ stacked vertically. For samples 1 and 2, no intermediate cleaning procedures were employed to remove any polymer residue. However, they were annealed later 200 °C for 5 h under vacuum. In the case of samples 3 and 4, we performed the AFM-based "nano-squeegee" procedure to optimally create clean interfaces.[49] This involves the use of a standard AFM tip to push out polymer residue deposited between the two TMDs in a vertical heterostructure. We were able to use the same method to also remove the surface residue present on the ML $MoSe_2$ flake, using a 7 N/m spring constant ACSTGG tip and a contact force of F = 140 nN. We confirm the success of our procedure by performing PL measurements before and after employing this routine (Supporting Information (Figure S8)). Bulk $NbSe_2$ is then brought into contact with the sample and immediately capped with a thin layer of hBN to protect from further degradation. Samples 3 and 4 were additionally vacuum annealed at 200 °C for 5 h under vacuum to observe changes in interfacial effects and related PL properties. Sample fabrication details for samples 5−10 are included in Supporting Information (Figure S1).

Experimental Setup. Low-temperature PL and Raman measurements were carried out on a home-built confocal microscope setup with 532 nm (2.4 μm spot size) laser excitation focused through a 0.42 NA, 50× long working-distance objective. The light is collected in a backscattering geometry, with the collection fiber coupled to a 500 mm focal length single spectrometer integrated with a liquid-N_2-cooled CCD detector. The samples were placed under vacuum and cooled in a closed cycle He-cooled cryostat (Montana Instruments Corporation) with a variable-temperature range from 4 K to 300 K. Raman measurements of $NbSe_2$ included in the Supporting Information (Figure S4) were carried out using the same collection scheme, however, the excitation path included a collection of Bragg grating notch filters to get us within 15 cm^{-1} of the laser line. The laser power for Raman measurements was kept below 300 μW as measured before the microscope objective.

DFT Calculations. The electronic structures of MLs $NbSe_2$, $MoSe_2$ and the heterostructures were investigated using the general potential linearized augmented plane-wave (LAPW) method[79] as implemented in the WIEN2K code.[80] The convergence of the calculations regarding the size of the basis set is achieved using an $R_{MT} \times K_{max}$ value of 7, where R_{MT} is the smallest atomic sphere radius in the unit cell and K_{max} is the magnitude of the largest K wave vector inside the first Brillouin zone (BZ). The Perdew−Burke−Ernzerhof generalized-gradient approximation (PBE-GGA)[81] is used to describe the exchange and correlation functional. A vacuum space larger than 20 Å is set to avoid the interaction between the two adjacent layers. The Monkhorst−Pack k-grid of 18 × 18 × 1 is adopted for the first BZ integral, and the convergence criterion for the charge difference was <0.0001e per unit cell. To correctly describe the vdW interactions, we employed empirical pairwise corrections proposed by Grimme[82] in terms of the DFT+D2 scheme. Structures were fully relaxed until the force on each atom was <0.01 eV/Å. The optimized lattice constants of $MoSe_2$ and $NbSe_2$ are 3.33 and 3.48 Å, in good agreement with the recent work.[25] Since there is a lattice mismatch between $MoSe_2$ and $NbSe_2$ MLs, $NbSe_2$ is applied a strain of −4.3% in the heterostructure.

ASSOCIATED CONTENT

Supporting Information

The Supporting Information is available free of charge at https://pubs.acs.org/doi/10.1021/acsnano.0c02803.

Experimental characterization of other heterostructure samples and origin of L1, Raman measurements of bulk $NbSe_2$, additional discussion on intralayer moiré excitons, DFT calculations of the vdW interaction between $NbSe_2$ and $MoSe_2$, and supplementary hyper-spectral reflectance contrast data (PDF)

AUTHOR INFORMATION

Corresponding Author

Patrick M. Vora − *Department of Physics and Astronomy and Quantum Science and Engineering Center, George Mason University, Fairfax, Virginia 22030, United States;* orcid.org/0000-0003-3967-8137; Email: pvora@gmu.edu

Authors

Jaydeep Joshi − *Department of Physics and Astronomy and Quantum Science and Engineering Center, George Mason University, Fairfax, Virginia 22030, United States;* orcid.org/0000-0002-8024-0586

Tong Zhou − *Department of Physics, University at Buffalo, Buffalo, New York 14260, United States*

Sergiy Krylyuk − *Materials Science and Engineering Division, National Institute of Standards and Technology, Gaithersburg, Maryland 20899, United States*

Albert V. Davydov − *Materials Science and Engineering Division, National Institute of Standards and Technology, Gaithersburg, Maryland 20899, United States;* orcid.org/0000-0003-4512-2311

Igor Žutić − *Department of Physics, University at Buffalo, Buffalo, New York 14260, United States*

Complete contact information is available at: https://pubs.acs.org/10.1021/acsnano.0c02803

Notes

Certain commercial equipment, instruments, or materials are identified in this paper in order to specify the experimental procedure adequately. Such identification is not intended to imply recommendation or endorsement by the National Institute of Standards and Technology, nor is it intended to imply that the materials or equipment identified are necessarily the best available for the purpose.

The authors declare no competing financial interest.

ACKNOWLEDGMENTS

P.M.V. and J.J. acknowledge support from the National Science Foundation (NSF) under grant nos. DMR-1748650 and DMR-1847782 and the George Mason University Quantum Science and Engineering Center. I.Z. and T.Z. acknowledge support from the U.S. Department of Energy, Office of Science, Basic Energy Sciences under award no. DE-SC0004890 and the University at Buffalo Center for Computational Research. This work is partly supported through the Material Genome Initiative funding allocated to NIST. The authors would further like to thank I. Mazin and A. Rigosi for valuable discussions.

REFERENCES

(1) Alferov, Z. I. Nobel Lecture: The Double Heterostructure Concept and Its Applications in Physics, Electronics, and Technology. *Rev. Mod. Phys.* **2001**, *73*, 767−782.

(2) Žutić, I.; Matos-Abiague, A.; Scharf, B.; Dery, H.; Belashchenko, K. Proximitized Materials. *Mater. Today* **2019**, *22*, 85−107.

(3) Choi, W.; Choudhary, N.; Han, G. H.; Park, J.; Akinwande, D.; Lee, Y. H. Recent Development of Two-Dimensional Transition Metal Dichalcogenides and Their Applications. *Mater. Today* **2017**, *20*, 116−130.

(4) Manzeli, S.; Ovchinnikov, D.; Pasquier, D.; Yazyev, O. V.; Kis, A. 2D Transition Metal Dichalcogenides. *Nat. Rev. Mater.* **2017**, *2*, 17033.

(5) Mak, K. F.; Shan, J. Photonics and Optoelectronics of 2D Semiconductor Transition Metal Dichalcogenides. *Nat. Photonics* **2016**, *10*, 216−226.

(6) Guguchia, Z.; Kerelsky, A.; Edelberg, D.; Banerjee, S.; von Rohr, F.; Scullion, D.; Augustin, M.; Scully, M.; Rhodes, D. A.; Shermadini, Z.; et al. Magnetism in Semiconducting Molybdenum Dichalcogenides. *Sci. Adv.* **2018**, *4*, No. eaat3672.

(7) Mak, K. F.; Lee, C.; Hone, J.; Shan, J.; Heinz, T. F. Atomically Thin MoS_2: A New Direct-Gap Semiconductor. *Phys. Rev. Lett.* **2010**, *105*, 136805.

(8) Chernikov, A.; Berkelbach, T. C.; Hill, H. M.; Rigosi, A.; Li, Y.; Aslan, O. B.; Reichman, D. R.; Hybertsen, M. S.; Heinz, T. F. Exciton Binding Energy and Nonhydrogenic Rydberg Series in Monolayer WS_2. *Phys. Rev. Lett.* **2014**, *113*, 076802.

(9) Wang, G.; Chernikov, A.; Glazov, M. M.; Heinz, T. F.; Marie, X.; Amand, T.; Urbaszek, B. Colloquium: Excitons in Atomically Thin Transition Metal Dichalcogenides. *Rev. Mod. Phys.* **2018**, *90*, 021001.

(10) Mueller, T.; Malic, E. Exciton Physics and Device Application of Two-Dimensional Transition Metal Dichalcogenide Semiconductors. *npj 2D Mater. Appl.* **2018**, *2*, 29.

(11) Xu, X.; Yao, W.; Xiao, D.; Heinz, T. F. Spin and Pseudospins in Layered Transition Metal Dichalcogenides. *Nat. Phys.* **2014**, *10*, 343−350.

(12) Jariwala, D.; Marks, T. J.; Hersam, M. C. Mixed-Dimensional van der Waals Heterostructures. *Nat. Mater.* **2017**, *16*, 170−181.

(13) Liu, Y.; Weiss, N. O.; Duan, X.; Cheng, H.-C.; Huang, Y.; Duan, X. Van der Waals Heterostructures and Devices. *Nat. Rev. Mater.* **2016**, *1*, 16042.

(14) Liu, H.; Neal, A. T.; Ye, P. D. Channel Length Scaling of MoS_2 MOSFETs. *ACS Nano* **2012**, *6*, 8563−8569.

(15) Das, S.; Appenzeller, J. WSe_2 Field Effect Transistors with Enhanced Ambipolar Characteristics. *Appl. Phys. Lett.* **2013**, *103*, 103501.

(16) Larentis, S.; Fallahazad, B.; Tutuc, E. Field-Effect Transistors and Intrinsic Mobility in Ultra-Thin $MoSe_2$ Layers. *Appl. Phys. Lett.* **2012**, *101*, 223104.

(17) Das, S.; Chen, H. Y.; Penumatcha, A. V.; Appenzeller, J. High Performance Multilayer MoS_2 Transistors with Scandium Contacts. *Nano Lett.* **2013**, *13*, 100−105.

(18) Bhanu, U.; Islam, M. R.; Tetard, L.; Khondaker, S. I. Photoluminescence Quenching in Gold - MoS_2 Hybrid Nanoflakes. *Sci. Rep.* **2015**, *4*, 5575.

(19) Froehlicher, G.; Lorchat, E.; Berciaud, S. Charge *versus* Energy Transfer in Atomically Thin Graphene-Transition Metal Dichalcogenide van der Waals Heterostructures. *Phys. Rev. X* **2018**, *8*, 011007.

(20) Zhang, L.; Yan, H.; Sun, X.; Dong, M.; Yildirim, T.; Wang, B.; Wen, B.; Neupane, G. P.; Sharma, A.; Zhu, Y.; et al. Modulated Interlayer Charge Transfer Dynamics in a Monolayer TMD/Metal Junction. *Nanoscale* **2019**, *11*, 418−425.

(21) Guan, J.; Chuang, H. J.; Zhou, Z.; Tománek, D. Optimizing Charge Injection across Transition Metal Dichalcogenide Heterojunctions: Theory and Experiment. *ACS Nano* **2017**, *11*, 3904−3910.

(22) Shin, H. G.; Yoon, H. S.; Kim, J. S.; Kim, M.; Lim, J. Y.; Yu, S.; Park, J. H.; Yi, Y.; Kim, T.; Jun, S. C.; et al. Vertical and In-Plane Current Devices Using NbS_2/n-MoS_2 van der Waals Schottky Junction and Graphene Contact. *Nano Lett.* **2018**, *18*, 1937−1945.

(23) Dvir, T.; Massee, F.; Attias, L.; Khodas, M.; Aprili, M.; Quay, C. H. L.; Steinberg, H. Spectroscopy of Bulk and Few-Layer Superconducting $NbSe_2$ with van der Waals Tunnel Junctions. *Nat. Commun.* **2018**, *9*, 598.

(24) Huang, C.; Narayan, A.; Zhang, E.; Liu, Y.; Yan, X.; Wang, J.; Zhang, C.; Wang, W.; Zhou, T.; Yi, C.; et al. Inducing Strong Superconductivity in WTe_2 by a Proximity Effect. *ACS Nano* **2018**, *12*, 7185−7196.

(25) Lv, X.; Wei, W.; Zhao, P.; Li, J.; Huang, B.; Dai, Y. Tunable Schottky Contacts in MSe_2/$NbSe_2$ (M = Mo and W) Heterostructures and Promising Application Potential in Field-Effect Transistors. *Phys. Chem. Chem. Phys.* **2018**, *20*, 1897−1903.

(26) Yabuki, N.; Moriya, R.; Arai, M.; Sata, Y.; Morikawa, S.; Masubuchi, S.; Machida, T. Supercurrent in van der Waals Josephson Junction. *Nat. Commun.* **2016**, *7*, 10616.

(27) Lee, J.; Kim, M.; Watanabe, K.; Taniguchi, T.; Lee, G. H.; Lee, H. J. Planar Graphene Josephson Coupling *via* van der Waals Superconducting Contacts. *Curr. Appl. Phys.* **2019**, *19*, 251−255.

(28) Kim, M.; Park, G. H.; Lee, J.; Lee, J. H.; Park, J.; Lee, H.; Lee, G. H.; Lee, H. J. Strong Proximity Josephson Coupling in Vertically Stacked $NbSe_2$-Graphene-$NbSe_2$ van der Waals Junctions. *Nano Lett.* **2017**, *17*, 6125−6130.

(29) Pan, Y.; Li, S.; Ye, M.; Quhe, R.; Song, Z.; Wang, Y.; Zheng, J.; Pan, F.; Guo, W.; Yang, J.; et al. Interfacial Properties of Monolayer $MoSe_2$-Metal Contacts. *J. Phys. Chem. C* **2016**, *120*, 13063−13070.

(30) Liu, S.; Li, J.; Shi, B.; Zhang, X.; Pan, Y.; Ye, M.; Quhe, R.; Wang, Y.; Zhang, H.; Yan, J.; et al. Gate-Tunable Interfacial Properties of In-Plane ML MX_2 1T'−2H Heterojunctions. *J. Mater. Chem. C* **2018**, *6*, 5651−5661.

(31) Çakir, D.; Sevik, C.; Peeters, F. M. Engineering Electronic Properties of Metal-$MoSe_2$ Interfaces Using Self-Assembled Monolayers. *J. Mater. Chem. C* **2014**, *2*, 9842−9849.
(32) Huang, L.; Li, B.; Zhong, M.; Wei, Z.; Li, J. Tunable Schottky Barrier at $MoSe_2$/Metal Interfaces with a Buffer Layer. *J. Phys. Chem. C* **2017**, *121*, 9305−9311.
(33) Liu, Y.; Stradins, P.; Wei, S.-H. Van der Waals Metal-Semiconductor junction: Weak Fermi Level Pinning Enables Effective Tuning of Schottky Barrier. *Sci. Adv.* **2016**, *2*, No. e1600069.
(34) Mönch, W. Barrier Heights of Real Schottky Contacts Explained by Metal-Induced Gap States and Lateral Inhomogeneities. *J. Vac. Sci. Technol., B: Microelectron. Process. Phenom.* **1999**, *17*, 1867.
(35) Heine, V. Theory of Surface States. *Phys. Rev.* **1965**, *138*, A1689−A1696.
(36) Sajjad, M.; Yang, X.; Altermatt, P.; Singh, N.; Schwingenschlögl, U.; De Wolf, S. Metal-Induced Gap States in Passivating Metal/Silicon Contacts. *Appl. Phys. Lett.* **2019**, *114*, 071601.
(37) Lu, C. P.; Li, G.; Mao, J.; Wang, L. M.; Andrei, E. Y. Bandgap, Mid-Gap States, and Gating Effects in MoS_2. *Nano Lett.* **2014**, *14*, 4628−4633.
(38) Scharf, B.; Van Tuan, D.; Žutić, I.; Dery, H. Dynamical Screening in Monolayer Transition-Metal Dichalcogenides and Its Manifestations in the Exciton Spectrum. *J. Phys.: Condens. Matter* **2019**, *31*, 203001.
(39) Ross, J. S.; Wu, S.; Yu, H.; Ghimire, N. J.; Jones, A. M.; Aivazian, G.; Yan, J.; Mandrus, D. G.; Xiao, D.; Yao, W.; et al. Electrical Control of Neutral and Charged Excitons in a Monolayer Semiconductor. *Nat. Commun.* **2013**, *4*, 1474.
(40) Edelberg, D.; Rhodes, D.; Kerelsky, A.; Kim, B.; Wang, J.; Zangiabadi, A.; Kim, C.; Abhinandan, A.; Ardelean, J.; Scully, M.; et al. Approaching the Intrinsic Limit in Transition Metal Diselenides *via* Point Defect Control. *Nano Lett.* **2019**, *19*, 4371−4379.
(41) Lu, Z.; Rhodes, D.; Li, Z.; Van Tuan, D.; Jiang, Y.; Ludwig, J.; Jiang, Z.; Lian, Z.; Shi, S.-F.; Hone, J.; et al. Magnetic Field Mixing and Splitting of Bright and Dark Excitons in Monolayer $MoSe_2$. *2D Mater.* **2020**, *7*, 015017.
(42) Ajayi, O. A.; Ardelean, J. V.; Shepard, G. D.; Wang, J.; Antony, A.; Taniguchi, T.; Watanabe, K.; Heinz, T. F.; Strauf, S.; Zhu, X.-Y.; et al. Approaching the Intrinsic Photoluminescence Linewidth in Transition Metal Dichalcogenide Monolayers. *2D Mater.* **2017**, *4*, 031011.
(43) Wierzbowski, J.; Klein, J.; Sigger, F.; Straubinger, C.; Kremser, M.; Taniguchi, T.; Watanabe, K.; Wurstbauer, U.; Holleitner, A. W.; Kaniber, M.; et al. Direct Exciton Emission from Atomically Thin Transition Metal Dichalcogenide Heterostructures near the Lifetime Limit. *Sci. Rep.* **2017**, *7*, 12383.
(44) Jadczak, J.; Kutrowska-Girzycka, J.; Kapuściński, P.; Huang, Y. S.; Wójs, A.; Bryja, L. Probing of Free and Localized Excitons and Trions in Atomically Thin WSe_2, WS_2, $MoSe_2$ and MoS_2 in Photoluminescence and Reflectivity Experiments. *Nanotechnology* **2017**, *28*, 395702.
(45) Van Tuan, D.; Yang, M.; Dery, H. Coulomb Interaction in Monolayer Transition-Metal Dichalcogenides. *Phys. Rev. B: Condens. Matter Mater. Phys.* **2018**, *98*, 125308.
(46) Florian, M.; Hartmann, M.; Steinhoff, A.; Klein, J.; Holleitner, A. W.; Finley, J. J.; Wehling, T. O.; Kaniber, M.; Gies, C. The Dielectric Impact of Layer Distances on Exciton and Trion Binding Energies in van der Waals Heterostructures. *Nano Lett.* **2018**, *18*, 2725−2732.
(47) Zhang, N.; Surrente, A.; Baranowski, M.; Maude, D. K.; Gant, P.; Castellanos-Gomez, A.; Plochocka, P. Moiré Intralayer Excitons in a $MoSe_2$/MoS_2 Heterostructure. *Nano Lett.* **2018**, *18*, 7651−7657.
(48) Lien, D.-H.; Kang, J. S.; Amani, M.; Chen, K.; Tosun, M.; Wang, H.-P.; Roy, T.; Eggleston, M. S.; Wu, M. C.; Dubey, M.; et al. Engineering Light Outcoupling in 2D Materials. *Nano Lett.* **2015**, *15*, 1356−1361.
(49) Rosenberger, M. R.; Chuang, H. J.; McCreary, K. M.; Hanbicki, A. T.; Sivaram, S. V.; Jonker, B. T. Nano-"Squeegee" for the Creation of Clean 2D Material Interfaces. *ACS Appl. Mater. Interfaces* **2018**, *10*, 10379−10387.
(50) Khestanova, E.; Guinea, F.; Fumagalli, L.; Geim, A. K.; Grigorieva, I. V. Universal Shape and Pressure inside Bubbles Appearing in van der Waals Heterostructures. *Nat. Commun.* **2016**, *7*, 12587.
(51) Frisenda, R.; Navarro-Moratalla, E.; Gant, P.; Pérez De Lara, D.; Jarillo-Herrero, P.; Gorbachev, R. V.; Castellanos-Gomez, A. Recent Progress in the Assembly of Nanodevices and van der Waals Heterostructures by Deterministic Placement of 2D Materials. *Chem. Soc. Rev.* **2018**, *47*, 53−68.
(52) Onodera, M.; Masubuchi, S.; Moriya, R.; Machida, T. Assembly of van der Waals Heterostructures: Exfoliation, Searching, and Stacking of 2D Materials. *Jpn. J. Appl. Phys.* **2020**, *59*, 010101.
(53) Tyurnina, A. V.; Bandurin, D. A.; Khestanova, E.; Kravets, V. G.; Koperski, M.; Guinea, F.; Grigorenko, A. N.; Geim, A. K.; Grigorieva, I. V. Strained Bubbles in van der Waals Heterostructures as Local Emitters of Photoluminescence with Adjustable Wavelength. *ACS Photonics* **2019**, *6*, 516−524.
(54) Branny, A.; Wang, G.; Kumar, S.; Robert, C.; Lassagne, B.; Marie, X.; Gerardot, B. D.; Urbaszek, B. Discrete Quantum Dot Like Emitters in Monolayer $MoSe_2$: Spatial Mapping, Magneto-Optics, and Charge Tuning. *Appl. Phys. Lett.* **2016**, *108*, 142101.
(55) Aas, S.; Bulutay, C. Strain Dependence of Photoluminescence and Circular Dichroism in Transition Metal Dichalcogenides: a $k \cdot p$ Analysis. *Opt. Express* **2018**, *26*, 28672.
(56) Hao, K.; Specht, J. F.; Nagler, P.; Xu, L.; Tran, K.; Singh, A.; Dass, C. K.; Schüller, C.; Korn, T.; Richter, M.; et al. Neutral and Charged Inter-Valley Biexcitons in Monolayer $MoSe_2$. *Nat. Commun.* **2017**, *8*, 15552.
(57) Hanbicki, A. T.; Chuang, H.-J.; Rosenberger, M. R.; Hellberg, C. S.; Sivaram, S. V.; McCreary, K. M.; Mazin, I. I.; Jonker, B. T. Double Indirect Interlayer Exciton in a $MoSe_2$/WSe_2 van der Waals Heterostructure. *ACS Nano* **2018**, *12*, 4719−4726.
(58) Island, J. O.; Kuc, A.; Diependaal, E. H.; Bratschitsch, R.; Van Der Zant, H. S.; Heine, T.; Castellanos-Gomez, A. Precise and Reversible Band Gap Tuning in Single-Layer $MoSe_2$ by Uniaxial Strain. *Nanoscale* **2016**, *8*, 2589−2593.
(59) Kang, J.; Tongay, S.; Zhou, J.; Li, J.; Wu, J. Band Offsets and Heterostructures of Two-Dimensional Semiconductors. *Appl. Phys. Lett.* **2013**, *102*, 012111.
(60) Zhang, Q.; Zhang, S.; Sperling, B. A.; Nguyen, N. V. Band Offset and Electron Affinity of Monolayer $MoSe_2$ by Internal Photoemission. *J. Electron. Mater.* **2019**, *48*, 6446−6450.
(61) Shimada, T.; Ohuchi, F. S.; Parkinson, B. A. Work Function and Photothreshold of Layered Metal Dichalcogenides. *Jpn. J. Appl. Phys.* **1994**, *33*, 2696.
(62) Yuan, Y. R.; Pudensi, M. A. A.; Vawter, G. A.; Merz, J. L. New Photoluminescence Effects of Carrier Confinement at an AlGaAs/GaAs HerojunctionInterface. *J. Appl. Phys.* **1985**, *58*, 397−403.
(63) Feng, J.; Qian, X.; Huang, C. W.; Li, J. Strain-Engineered Artificial Atom as a Broad-Spectrum Solar Energy Funnel. *Nat. Photonics* **2012**, *6*, 866−872.
(64) Castellanos-Gomez, A.; Roldán, R.; Cappelluti, E.; Buscema, M.; Guinea, F.; van der Zant, H. S. J.; Steele, G. A. Local Strain Engineering in Atomically Thin MoS_2. *Nano Lett.* **2013**, *13*, 5361−5366.
(65) Barbone, M.; Montblanch, A. R.-P.; Kara, D. M.; Palacios-Berraquero, C.; Cadore, A. R.; De Fazio, D.; Pingault, B.; Mostaani, E.; Li, H.; Chen, B.; et al. Charge-Tuneable Biexciton Complexes in Monolayer WSe_2. *Nat. Commun.* **2018**, *9*, 3721.
(66) Shibata, H.; Sakai, M.; Yamada, A.; Matsubara, K.; Sakurai, K.; Tampo, H.; Ishizuka, S.; Kim, K.-K.; Niki, S. Excitation-Power Dependence of Free Exciton Photoluminescence of Semiconductors. *Jpn. J. Appl. Phys.* **2005**, *44*, 6113−6114.
(67) Yu, H.; Liu, G.-B.; Tang, J.; Xu, X.; Yao, W. Moiré excitons: From Programmable Quantum Emitter Arrays to Spin-Orbit−Coupled Artificial L attices. *Sci. Adv.* **2017**, *3*, No. e1701696.

https://dx.doi.org/10.1021/acsnano.0c02803
ACS Nano 2020, 14, 8528−8538

(68) Wu, F.; Lovorn, T.; MacDonald, A. H. Topological Exciton Bands in Moiré Heterojunctions. *Phys. Rev. Lett.* **2017**, *118*, 147401.
(69) Shibata, H. Negative Thermal Quenching Curves in Photoluminescence of Solids. *Jpn. J. Appl. Phys.* **1998**, *37*, 550−553.
(70) Huang, J.; Hoang, T. B.; Mikkelsen, M. H. Probing the Origin of Excitonic States in Monolayer WSe_2. *Sci. Rep.* **2016**, *6*, 22414.
(71) Lin, S. S.; Chen, B. G.; Xiong, W.; Yang, Y.; He, H. P.; Luo, J. Negative Thermal Quenching of Photoluminescence in Zinc Oxide Nanowire-Core/Graphene-Shell Complexes. *Opt. Express* **2012**, *20*, A706.
(72) Mouri, S.; Zhang, W.; Kozawa, D.; Miyauchi, Y.; Eda, G.; Matsuda, K. Thermal Dissociation of Inter-Layer Excitons in MoS_2/$MoSe_2$ Hetero-bilayers. *Nanoscale* **2017**, *9*, 6674−6679.
(73) Chen, S.-Y.; Goldstein, T.; Taniguchi, T.; Watanabe, K.; Yan, J. Coulomb-Bound Four- and Five-Particle Intervalley States in an Atomically-Thin Semiconductor. *Nat. Commun.* **2018**, *9*, 3717.
(74) O'Donnell, K. P.; Chen, X. Temperature Dependence of Semiconductor Band Gaps. *Appl. Phys. Lett.* **1991**, *58*, 2924−2926.
(75) Coldren, L. A.; Corzine, S. W.; Mašanović, M. L. *Diode Lasers and Photonic Integrated Circuits*, 2nd ed.; John Wiley & Sons, Inc.: Hoboken, NJ, 2012; p 752.
(76) Chuang, S. L. *Physics of Photonic Devices*, 2nd ed.; Wiley: Hoboken, NJ, 2009; p 840.
(77) Lindemann, M.; Xu, G.; Pusch, T.; Michalzik, R.; Hofmann, M. R.; Žutić, I.; Gerhardt, N. C. Ultrafast Spin-Lasers. *Nature* **2019**, *568*, 212−215.
(78) Castellanos-Gomez, A.; Buscema, M.; Molenaar, R.; Singh, V.; Janssen, L.; van der Zant, H. S. J.; Steele, G. A. Deterministic Transfer of Two-Dimensional Materials by All-Dry Viscoelastic Stamping. *2D Mater.* **2014**, *1*, 011002.
(79) Singh, D. J.; Nordstrom, L. *Planewaves, Pseudopotentials and the LAPW Method*, 2nd ed.; Springer US: Boston, MA, 2006; p 147.
(80) Blaha, P.; Schwarz, K.; Madsen, G. K. H.; Kvasnicka, D.; Luitz, J.; Laskowski, R.; Tran, F.; Marks, L. D. *WIEN2k: An Augmented Plane Wave Plus Local Orbitals Program for Calculating Crystal Properties*; Technical University of Berlin: Berlin, Germany, 2001; p 287.
(81) Perdew, J. P.; Burke, K.; Ernzerhof, M. Generalized Gradient Approximation Made Simple. *Phys. Rev. Lett.* **1996**, *77*, 3865−3868.
(82) Grimme, S. Semiempirical GGA-Type Density Functional Constructed with a Long-Range Dispersion Correction. *J. Comput. Chem.* **2006**, *27*, 1787−1799.

NOTE ADDED AFTER ASAP PUBLICATION

A partially corrected version of this paper was published on July 13, 2020 and the fully corrected version was reposted on July 16, 2020.

https://dx.doi.org/10.1021/acsnano.0c02803
ACS Nano 2020, 14, 8528−8538